mater.scichina.com link.springer.com

Published online 6 February 2023 | https://doi.org/10.1007/s40843-022-2348-9
Sci China Mater 2023, 66(5): 2032–2038

Record-high mobility and extreme magnetoresistance on kagome-lattice in compensated semimetal $Ni_3In_2S_2$

Hongwei Fang[1,2†], Meng Lyu[3†], Hao Su[1,2], Jian Yuan[1,2], Yiwei Li[1], Lixuan Xu[4], Shuai Liu[1,2], Liyang Wei[1,2], Xinqi Liu[1,5], Haifeng Yang[1], Qi Yao[1,5], Meixiao Wang[1,5], Yanfeng Guo[1], Wujun Shi[6,7*], Yulin Chen[1,5,8*], Enke Liu[3*] and Zhongkai Liu[1,5*]

ABSTRACT **The kagome-lattice crystal hosts various intriguing properties including the frustrated magnetism, charge order, topological state, superconductivity and correlated phenomena. To achieve high-performance kagome-lattice compounds for electronic and spintronic applications, careful tuning of the band structure would be desired. Here, the electronic structures of kagome-lattice crystal $Ni_3In_2S_2$ were investigated by transport measurements, angle-resolved photoemission spectroscopy as well as *ab initio* calculations. The transport measurements reveal $Ni_3In_2S_2$ as a compensated semimetal with record-high carrier mobility (~8683 and 7356 $cm^2 V^{-1} S^{-1}$ for holes and electrons) and extreme magnetoresistance (15,518% at 2 K and 13 T) among kagome-lattice materials. These extraordinary properties are well explained by its band structure with indirect gap, small electron/hole pockets and large bandwidth of the 3d electrons of Ni on the kagome lattice. This work demonstrates that the crystal field and doping serve as the key tuning knobs to optimize the transport properties in kagome-lattice crystals. Our work provides material basis and optimization routes for kagome-lattice semimetals towards electronics and spintronics applications.**

Keywords: kagome-lattice, high mobility, extreme magnetoresistance, compensated semimetal, electronic band structure

INTRODUCTION

In recent years, kagome-lattice crystals have attracted great research interest due to their unique magnetic and electronic properties [1–5]. The kagome-lattice crystals are an ideal platform to seek for the quantum spin liquid ground states due to the large geometric frustrations [1,6–10]; the kagome-lattice could host Dirac cone-type dispersions similar to the honeycomb lattice [11–13], flat bands due to the completely destructive interference of Bloch wave functions [11,13,14], topological electronic states (e.g., Weyl cones and topological surfaces states) as well as electronic instabilities such as charge density waves and superconductivity [15–19]. These unique properties render kagome-lattice compounds fascinating candidates for electronic and spintronic applications.

For device applications, high-performance kagome-lattice compounds (such as high carrier mobility, robust magnetism, and high transition temperature (T_c) superconductivity) are highly desired [20–23]. As an example, kagome-lattice naturally hosts fast-moving Dirac fermions which are feasible for high-mobility electronic devices [12–14]. However, the typical mobility of existing kagome-lattice crystals is ~100 to 1000 $cm^2 V^{-1} s^{-1}$ [20,24,25], much smaller than those of the typical Dirac electron systems (such as graphene, ~10^4 $cm^2 V^{-1} s^{-1}$) [26–28] and high-performance metal-oxide-semiconductor field-effect transistor materials (e.g., GaAs, ~10^4 $cm^2 V^{-1} s^{-1}$) [29–31]. Therefore, careful material optimization and tuning of the band structure would be a necessity to achieve kagome-lattice crystals with superior transport properties and facilitate the applications of kagome-lattice materials in electronic and spintronic devices.

Among the kagome-lattice compounds, the great tunability of the 3d transition metal intermetallic compounds provides a versatile platform for the search and optimization of the physical properties in kagome-lattice crystals, including FeSn, CoSn, and YMn_6Sn_6 [11,13,14]. In this work, we demonstrate such an effort in the kagome-lattice shandite $Ni_3In_2S_2$, a non-magnetic isostructural counterpart of the recently discovered magnetic topological Weyl semimetal (WSM) $Co_3Sn_2S_2$ [15,16,32,33]. With Ni substituting Co and In for Sn, we effectively tailor the band structure and achieve record-high mobility (~8683 and 7356 $cm^2 V^{-1} S^{-1}$ for holes and electrons) and electron-hole compensated extremely large and unsaturated magnetoresistance (MR) (15,518% at 2 K and 13 T) among all the existing

[1] School of Physical Science and Technology, ShanghaiTech University, Shanghai 201210, China
[2] University of Chinese Academy of Sciences, Beijing 100049, China
[3] Beijing National Laboratory for Condensed Matter Physics, Institute of Physics, Chinese Academy of Sciences, Beijing 100190, China
[4] State Key Laboratory of Low Dimensional Quantum Physics, Department of Physics, Tsinghua University, Beijing 100084, China
[5] ShanghaiTech Laboratory for Topological Physics, ShanghaiTech University, Shanghai 201210, China
[6] Center for Transformative Science, ShanghaiTech University, Shanghai 201210, China
[7] Shanghai High Repetition Rate XFEL and Extreme Light Facility (SHINE), ShanghaiTech University, Shanghai 201210, China
[8] Department of Physics, University of Oxford, Oxford OX1 3PU, United Kingdom
† These authors contributed equally to this work.
* Corresponding authors (emails: shiwujun@shanghaitech.edu.cn (Shi W); yulin.chen@physics.ox.ac.uk (Chen Y); ekliu@iphy.ac.cn (Liu E); liuzhk@shanghaitech.edu.cn (Liu Z))

kagome-lattice crystals. *Via* band structure investigation and analysis using angle resolved photoemission spectroscopy (ARPES) and *ab initio* calculations, we attribute these superior transport properties to (1) the delicate band arrangement under the crystal field which forms a bandgap *via* the topological phase transition ($Co_3Sn_2S_2$ possesses inverted 3d bands) and restores the bandwidth of the Ni 3d electrons on the kagome-lattice, and (2) proper doping which forms small and compensated electron and hole pockets at the Fermi energy (E_F). Our results demonstrate a compensated semimetal $Ni_3In_2S_2$ with high mobility and extreme MR (XMR) and illustrate a possible route in the modification of the electronic structure of kagome-lattice compounds for achieving superior transport properties, which render them great potential in high-mobility electronic and spintronic applications.

EXPERIMENTAL SECTION

Crystal growth

Single crystals of $Ni_3In_2S_2$ were grown through the solid state chemical reaction route. Mixtures of high-purity elements Ni (Macklin, 99.99%), In (Aladdin, 99.99%) and Sulfur (Adamas, 99.999%) in a stoichiometric ratio were put into an alumina crucible and sealed inside an evacuated quartz tube. The assembly was heated up to 1000°C within 20 h in the furnace and held at 1000°C for 30 h. Then it is slowly cooled at a rate of 2°C h^{-1} to 500°C, followed by switching off the furnace to let the sample cool down to room temperature.

Electrical transport measurements

The electrical transport measurements were carried out in a physical property measurement system (PPMS, 14T) between 2 K and room temperature, using a sample with a typical dimension of 0.1 mm × 0.5 mm × 1.5 mm. A standard four-probe method was applied for the longitudinal resistivity and the Hall-effect measurements with a current along the *a*-axis and magnetic fields parallel to the *c*-axis. To eliminate the influence of misalignment of the lead contact, all XR- and Hall-effect measurements were conducted by scanning both negative and positive magnetic fields.

Angle-resolved photoemission spectroscopy

ARPES measurements were performed at the Beamline I05 of the Diamond Light Source (DLS) with a Scienta R4000 analyzer and Beamline BL03U of Shanghai Synchrotron Radiation Facility (SSRF) with a Scienta DA30 analyzer. The photon-energy ranges of data acquisition for DLS and SSRF were 52–200 and 58–114 eV, respectively. The samples were cleaved *in situ* at 23 K and measured in ultrahigh vacuum with a base pressure of less than 5 × 10^{-11} Torr (1 Torr = 133.322 Pa). The energy and momentum resolution were 10 meV and 0.2°, respectively.

Theoretical calculation

The first-principles calculations were performed using the Vienna *ab initio* Simulation Package (VASP) [34]. The interactions between the valence electrons and ion cores are described by the projector augmented wave method [35,36], and exchange-correlation potential was formulated by the generalized gradient approximation with the Perdew-Burke-Ernzerhof (PBE) scheme [34]. The Γ-centered 10 × 10 × 10 k points were used for the first Brillouin-zone sampling. The spin-orbit coupling (SOC) was included in all the calculations. The tight-binding Hamiltonian was constructed using the maximally localized Wannier functions which were provided by Wannier90 Package [37]. The surface states (SS) were calculated by the surface Green's function method [38] based the tight-binding Hamiltonian. The experiment lattice constant (Inorganic Crystal Structure Database No. 415258) was used in the calculations.

RESULTS AND DISCUSSION

First, we characterized the basic properties of $Ni_3In_2S_2$. $Ni_3In_2S_2$ has a rhombohedral lattice structure with the space group $R\bar{3}m$ (No. 166). The conventional cell and primitive cell are shown in Fig. 1a with the conventional lattice constants to be $a = b =$ 5.37 Å, c = 13.56 Å. The crystal is formed by sequenced In-[S-(Ni3-In)-S] layers along the *c* direction, where Ni atoms form a kagome-lattice (Fig. 1b) sandwiched between two hexagonal S atoms. The typical samples for our measurement have sizes around several millimeters and the high quality of the single-crystalline samples used in this work is demonstrated by the single-crystal X-ray diffraction (XRD) angle scan (Fig. 1c). Fig. 1d presents the temperature-dependent longitudinal resistivity $\rho_{xx}(T)$ under different magnetic fields. Upon cooling from room temperature to 2 K, the zero-field $\rho_{xx}(T)$ continuously decreases and then flattens at low temperatures, without any signature of phase transition, suggesting the absence of long-range magnetic order in $Ni_3In_2S_2$. Both the quite low residual resistivity of 0.018 μΩ cm and the large residual resistance ratio (RRR) of 215 reflect the very high quality of the studied crystal. Upon the increasing field, we noticed a significant upturn of the resistivity at low temperatures, which indicates a large MR effect of $Ni_3In_2S_2$, and further, a semi-metallic with small Fermi pockets. The similar low-temperature resistivity upturn behavior has also been observed in other semi-metallic compounds, such as TaAs, $PtBi_2$, and WP_2 [39–42]. In addition, the calculated three-dimensional (3D) Fermi surfaces are shown in Fig. 1e, f. Electron pockets near the Γ point and hole pockets near the W point were observed and the electron pockets and hole pockets possess similar volumes, demonstrating $Ni_3In_2S_2$ as a nearly compensated semimetal.

The above analysis hints the similar transport properties as nearly compensated semimetal and encourages us to explore the magneto-transport properties of $Ni_3In_2S_2$, which is summarized in Fig. 2. Fig. 2a shows the magnetic-field-dependent MR for $Ni_3In_2S_2$ single crystal at different temperatures. The MR is greatly enhanced with the applied external magnetic field along the *c*-axis direction, displaying no signature of saturation and reaching a high value of 15,518% at 2 K and 13 T, representing an XMR effect in a semimetal. This XMR effect is rarely observed in other kagome-lattice materials, suggesting the unique magneto-transport property in $Ni_3In_2S_2$. Upon raising the temperature, the MR decreases dramatically and becomes negligible at 50 K. In the inset of Fig. 2a, we fitted the MR at T = 2 K by AH^n where n is estimated to be 1.9, which further indicates $Ni_3In_2S_2$ may be a nearly compensated semimetal with high carrier mobility (the perfectly compensated semimetal with equal density of electron (n_e) and hole (n_h) type carriers gives MR = $\mu_e\mu_h H^2$, where μ_e/μ_h are the electron/hole mobility, respectively).

Furthermore, to evaluate the carrier-related parameters, we estimated the carrier density and mobility from the Hall resistivity (ρ_{yx}) and magneto-resistivity (ρ_{xx}) at different tempera-

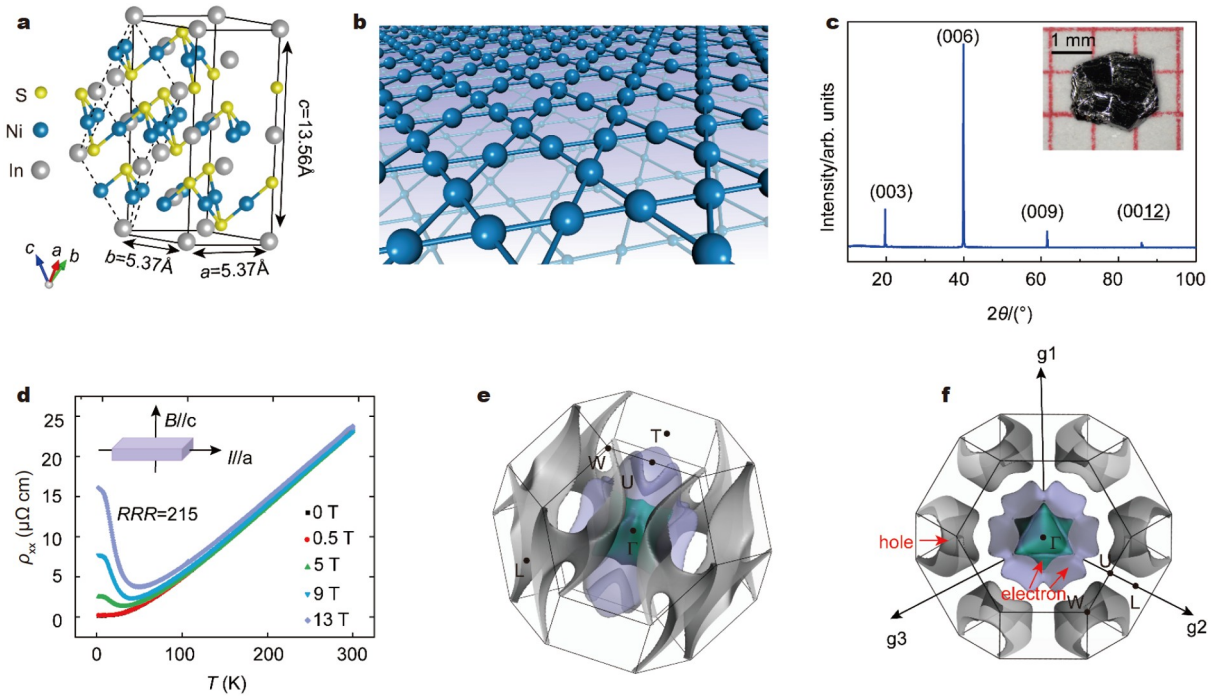

Figure 1 Basic characterization of $Ni_3In_2S_2$. (a) Conventional (solid lines) and primitive (dotted lines) cell of $Ni_3In_2S_2$. (b) Illustration of the kagome-lattice formed by Ni. (c) XRD pattern of $Ni_3In_2S_2$ measured at room temperature. Inset: photograph of the high-quality $Ni_3In_2S_2$ single crystal. (d) Temperature-dependent resistivity under different magnetic fields. Inset: configuration of the applied electrical current and magnetic fields. (e) 3D map and (f) top view of the calculated Fermi surface. Purple and green sheets represent electron pockets and gray sheets represent hole pockets.

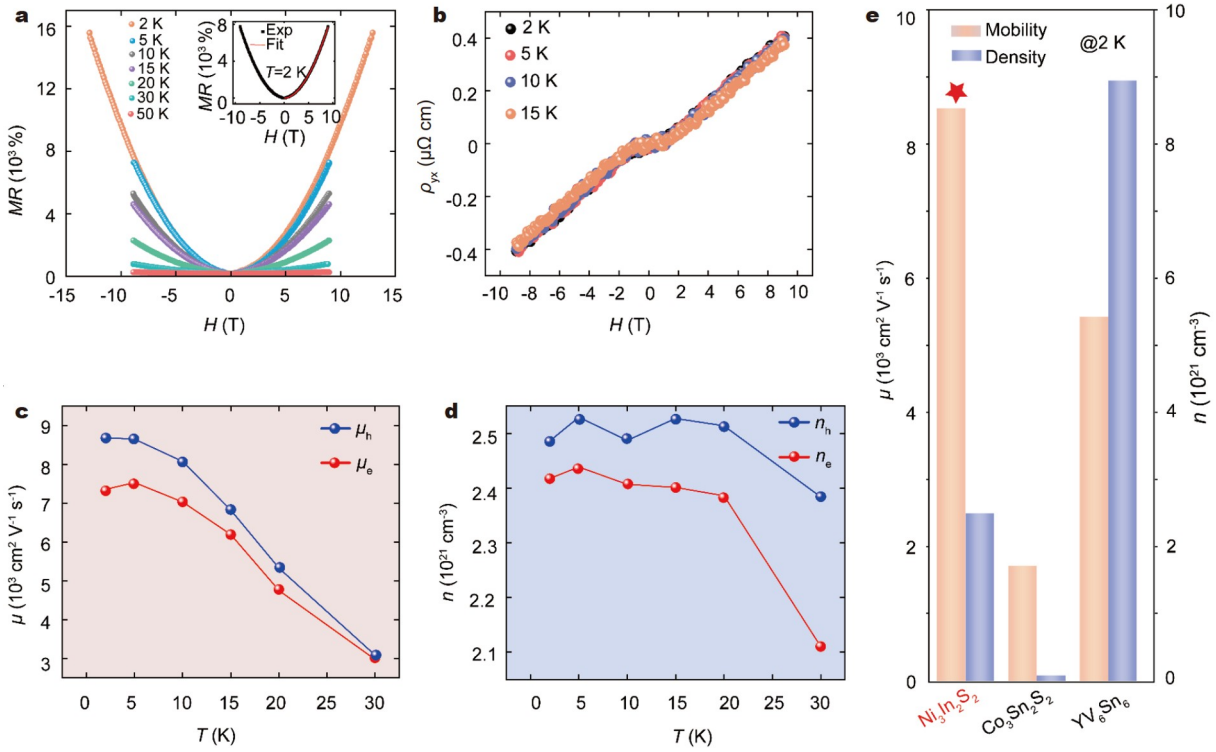

Figure 2 Magnetic transport measurement of $Ni_3In_2S_2$. (a) MR as a function of the magnetic field at 2–50 K. In the inset, the experimental data at 2 K have been fitted using MR = AH^n, yielding n = 1.9. (b) Hall resistivity as a function of magnetic field at different temperatures. (c) Carrier mobility as a function of temperature. (d) Carrier concentration as a function of temperature. (e) Comparison of carrier concentrations and mobilities of typical kagome-lattice materials. Data for other typical kagome-lattice materials are from Refs. [20,43].

tures. The ρ_{yx} at high temperatures is almost linear and positive, implying that the majority carrier is the hole type (see Supplementary information Fig. S1). Fig. 2b plots ρ_{yx} *vs.* magnetic field at various temperatures, which exhibits a nonlinear behavior and persists down to 2 K, reflecting the typical characteristic of multi-type carriers. We thus extracted the carrier density and mobility of $Ni_3In_2S_2$ at low temperatures using the two-band model, by simultaneously fitting:

$$\rho_{yx} = \frac{B}{e}\frac{\left(n_h\mu_h^2 - n_e\mu_e^2\right) + (n_h - n_e)\mu_h^2\mu_e^2B^2}{\left(n_h\mu_h + n_e\mu_e\right)^2 + (n_h - n_e)^2\mu_h^2\mu_e^2B^2},$$

$$\rho_{xx} = \frac{1}{e}\frac{\left(n_h\mu_h + n_e\mu_e\right) + \left(n_h\mu_e + n_e\mu_h\right)\mu_h\mu_eB^2}{\left(n_h\mu_h + n_e\mu_e\right)^2 + (n_h - n_e)^2\mu_h^2\mu_e^2B^2},$$

where $n_h(n_e)$ and $\mu_h(\mu_e)$ are the hole (electron) density and mobility, respectively, and B is the magnetic field. Fig. 2c and d display the fitting results of the mobility of the carriers and carrier density at different temperatures. At 2 K, n_h = 2.49 × 10^{21} cm^{-3} and n_e = 2.42 × 10^{21} cm^{-3}, which are quite close to each other, and are highly consistent with the results obtained by band calculations (n_h = 1.37 × 10^{21} cm^{-3} and n_e = 1.36 × 10^{21} cm^{-3}), respectively (the difference may be due to simplified nature of the two-band model). These results indicate $Ni_3In_2S_2$ is indeed a compensated semimetal. Besides, the hole and electron mobility at 2 K are 8683 and 7356 cm^2 V^{-1} s^{-1}, respectively, which are the highest values among all reported kagome-lattice materials (Fig. 2e) [20,43]. The large carrier mobility and compensated carrier concentration in turn explains the above mentioned XMR effect in this system, in the similar mechanism as proposed in compensated semimetals [44]. Interestingly, we note the mobility in $Ni_3In_2S_2$ is multiple times higher than that in the isostructural $Co_3Sn_2S_2$ [20], suggesting the role of crystal field and doping in tuning the band structure and the transport properties, as elaborated later. These excellent transport properties observed in $Ni_3In_2S_2$ could provide an ideal platform for studying the electronic transport behavior for advanced electronic or spintronic devices based on kagome physics.

In order to trace the origin of the high mobility and non-saturated XMR effect, we systematically investigated the electronic structure of $Ni_3In_2S_2$ by ARPES. The 3D Brillouin zone (BZ) of the primitive cell and the projected surface BZ of the conventional cell in the (001) plane are shown in Fig. 3a, with the momentum axis labelled. After cleaving, flat and shiny surface was created, ideal for ARPES measurement, and the high crystal quality was confirmed by the Laue pattern and the topography image of the cleaved surface measured by scanning tunneling microscopy (STM) (Fig. 3b), which confirmed the cleavage surface as the (001) surface. The measured high symmetry dispersion along the $\overline{K}-\overline{\Gamma}-\overline{K}$ and $\overline{M}-\overline{\Gamma}-\overline{M}$ derections are shown in Fig. 3c(i) and d(i). Due to the significant k_z broadening effect observed (see Supplementary information Fig. S2 for the photon-energy-dependent ARPES measurement),

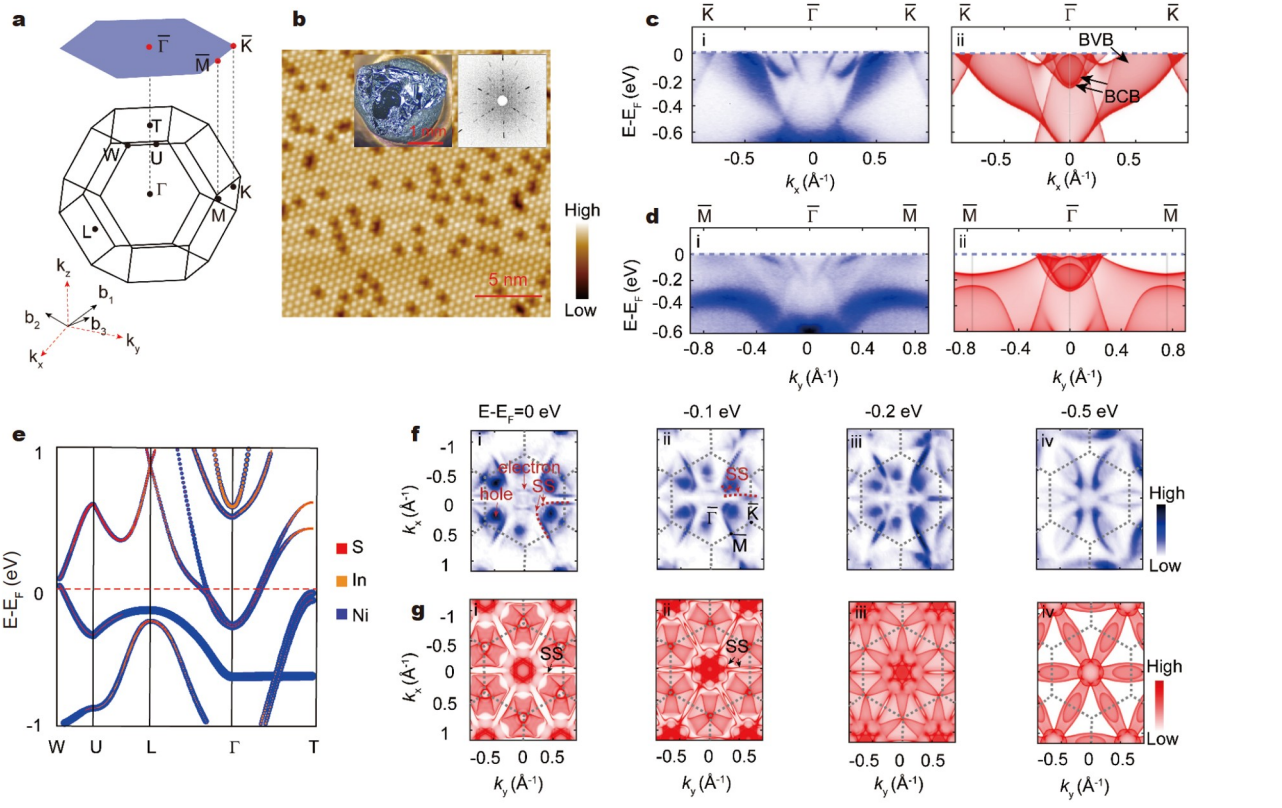

Figure 3 The electronic structure of $Ni_3In_2S_2$ measured by ARPES. (a) The bulk BZ and its projection on the (001) surface. (b) STM topography image of the cleaved (001) surface. Left inset: cleaved surface of $Ni_3In_2S_2$ single crystal. Right inset: Laue pattern showing the high quality of the $Ni_3In_2S_2$ crystal. (c) (i, ii) High-symmetry cut along the $\overline{K}-\overline{\Gamma}-\overline{K}$ direction and the corresponding calculated band dispersion. (d) (i, ii) High-symmetry cut along the $\overline{M}-\overline{\Gamma}-\overline{M}$ direction and the corresponding calculated band dispersion. Data are mirror symmetrized according to the crystal symmetry. (e) The calculated bulk band structure in the BZ of the primitive cell with their orbital compositions labelled in different colors. (f) (i–iv) Photoemission intensity maps of CECs at 0, 0.1, 0.2 and 0.5 eV below E_F, respectively. (g) (i–iv) Corresponding calculated CECs at the same energies. BCB: bulk conduction band; BVB: bulk valence band.

ARPES data captures both dispersions from Γ and T points. Therefore, hole pockets from W and electronic pockets from Γ (labeled as BVB/BCB in Fig. 3c(ii), see the calculated band structure in the primitive cell in Fig. 3e) are observed near $\overline{K}$ and $\overline{\Gamma}$, respectively, showing excellent agreement with the projected band structure from the slab calculations (Fig. 3c, d). The constant energy contours (CECs) further reveal clear hole pockets near $\overline{K}$ and electron pocket near $\overline{\Gamma}$ (Fig. 3f), identical to the calculation results in Fig. 3g (see detailed comparison in Fig. S3, which gives the estimate of 3D hole/electron concentration as n_h = 1.37 × 10^{21} cm^{-3} and n_e = 1.36 × 10^{21} cm^{-3}, respectively, further proving the electron-hole compensation nature in $Ni_3In_2S_2$). We also note the sharp SS near the $\overline{M}$ point chould be identified, contributing to the parallel lines near the $\overline{M}$ point (the SS are marked by the red arrows, see Fig. S4 for detail). The excellent agreement between experiments and calculations proves the validity of the calculation. Combining the transport and calculation results of the electron and hole concentrations, we further confirmed the nearly compensated semimetal nature in $Ni_3In_2S_2$, which is key to the high mobility and non-saturated XMR effect in $Ni_3In_2S_2$.

We interpret the superior transport behavior based on the calculated band structure as presented in Fig. 3e. The orbital analysis suggests the electron pockets near Γ and hole pockets near W originate from the Ni 3d orbitals on the kagome-lattice, which indicates that the excellent transport properties are closely related to the kagome structure. To further elaborate the relation between the unique electronic structure and the transport properties in $Ni_3In_2S_2$, we further performed systematic calculations on the band structure of four isostructural compounds: $Co_3Sn_2S_2$, $Ni_3Sn_2S_2$, $Ni_3In_2S_2$ and $Co_3In_2S_2$, and explore their band evolution to uncover the origin of the superior transport properties in $Ni_3In_2S_2$. As Fig. 4a–d show, in $Co_3Sn_2S_2$, $Ni_3Sn_2S_2$, and $Ni_3In_2S_2$, the d_{z^2} electron-like bands and $d_{x^2-y^2}$ hole-like bands are cutting through E_F, while the d_{z^2} hole-like bands dominate in $Co_3In_2S_2$ due to the lack of electrons. Due to the different crystal fields and spin orbit coupling strengths, there is clear band inversion between $d_{x^2-y^2}$ and d_{z^2}, leading to the topological WSM phase in the ferromagnetic $Co_3Sn_2S_2$ [32] and topological insulator (TI) phase in the paramagnetic $Ni_3Sn_2S_2$. The inverted band structure creates local band gaps and reduces the band width of the $d_{x^2-y^2}$ and d_{z^2} bands. In $Ni_3In_2S_2$ and $Co_3In_2S_2$, the band inversion between $d_{x^2-y^2}$ and d_{z^2} was cancelled and their bandwidth restored, leading to an indirect semiconductor-like gap around the Fermi level and allowing fast moving carriers from the spherical Fermi surfaces in indirect gaps (Fig. 4e). These characteristic carriers bring about high mobility, long mean free path, and XMR effect. Meanwhile, the different valence electrons in Co/Ni and In/Sn tune the Fermi level and control the carrier concentration. In $Co_3Sn_2S_2$, $Ni_3Sn_2S_2$ and $Ni_3In_2S_2$, the calculated concentrations of electron/hole carriers are less than the 2 × 10^{21} cm^{-3} and almost compensated, while in $Co_3In_2S_2$, the hole type carrier dominates and has a concentration of 8 × 10^{21} cm^{-3} (Fig. 4f). Combining the bandwidth and E_F position together, $Ni_3In_2S_2$ is the optimal system among the family with large bandwidth, small carrier concentration and compensated carrier, which explains its excellent high mobility and non-saturated XMR effect.

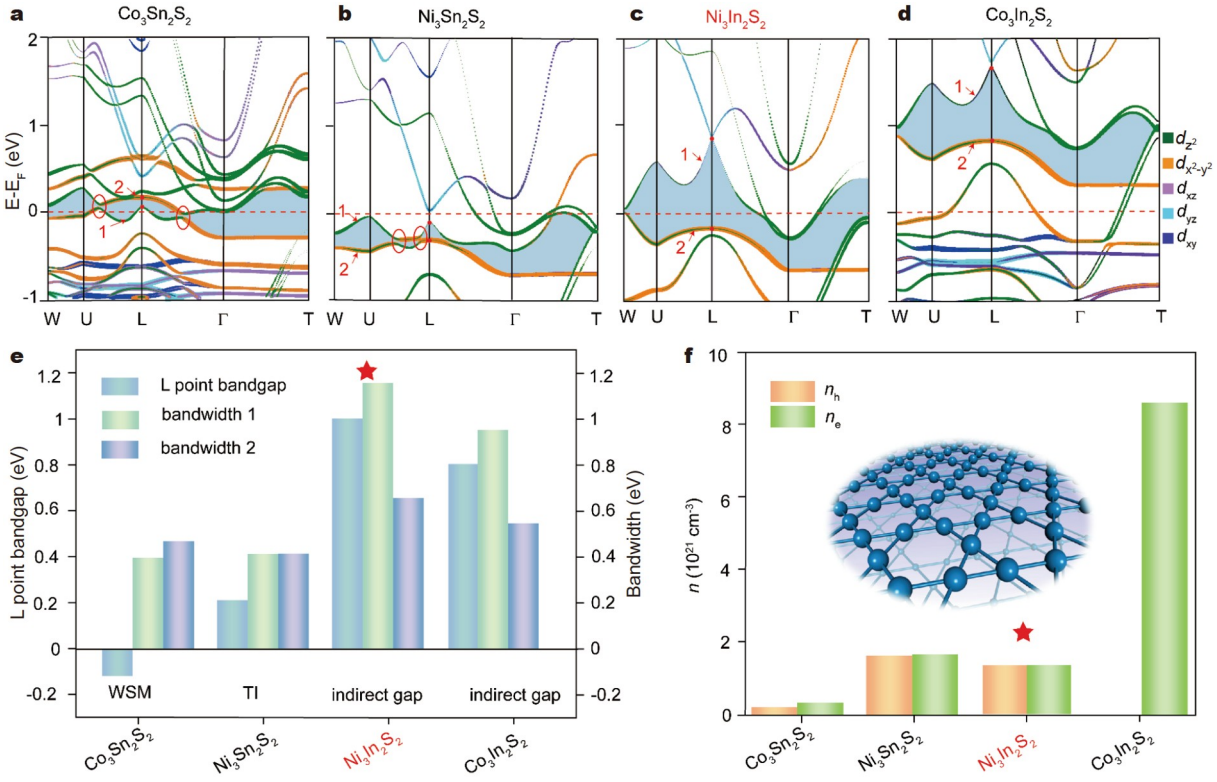

Figure 4 Electronic origin of the transport properties in $Ni_3Sn_2S_2$. (a–d) Plots of the projected band structure of Co/Ni 3d orbitals for $Co_3Sn_2S_2$, $Ni_3Sn_2S_2$, $Ni_3In_2S_2$, and $Co_3In_2S_2$, respectively. 1 and 2 label the bands with d_{z^2} and $d_{x^2-y^2}$ orbitals, and red circles indicate the band inversion points. Shaded area indicates the local band gaps between bands 1 and 2. (e) Summary of the local band gap between bands 1 and 2 at the L point, and bandwidths of 1 and 2 bands for the four compounds. (f) Summary of the carrier concentrations for the four compounds.

CONCLUSIONS

In summary, we have investigated the kagome-lattice material $Ni_3In_2S_2$ by magneto-transport measurement and electronic structure analysis. Our results reveal the high-mobility and non-saturated XMR in this compound which could be explained by the large bandwidth and electronic structure in compensated semimetal with an indirect gap. Such superior property could be attributed to the crystal field and spin-orbit interaction strength which controls the bandwidth *via* the topological phase transition, as well as the chemical doping which tunes the carrier type and concentration. Our results illustrate the key tuning knob of the electronic structure and key transport properties in the kagome-lattice crystals. $(Co,Ni)_3(Sn,In)_2S_2$ provides an ideal platform to investigate magnetism and topological property, as well as achieve high-mobility electronic and spintronic applications in kagome-lattice materials.

Received 10 October 2022; accepted 2 December 2022; published online 6 February 2023

1 Fu M, Imai T, Han TH, *et al.* Evidence for a gapped spin-liquid ground state in a kagome Heisenberg antiferromagnet. Science, 2015, 350: 655–658
2 Xue H, Yang Y, Gao F, *et al.* Acoustic higher-order topological insulator on a kagome lattice. Nat Mater, 2019, 18: 108–112
3 Guguchia Z, Verezhak JAT, Gawryluk DJ, *et al.* Tunable anomalous hall conductivity through volume-wise magnetic competition in a topological kagome magnet. Nat Commun, 2020, 11: 559
4 Denner MM, Thomale R, Neupert T. Analysis of charge order in the kagome metal AV_3Sb_5 (A = K, Rb, Cs). Phys Rev Lett, 2021, 127: 217601
5 Chisnell R, Helton JS, Freedman DE, *et al.* Topological magnon bands in a kagome lattice ferromagnet. Phys Rev Lett, 2015, 115: 147201
6 Han TH, Helton JS, Chu S, *et al.* Fractionalized excitations in the spin-liquid state of a kagome-lattice antiferromagnet. Nature, 2012, 492: 406–410
7 Yan S, Huse DA, White SR. Spin-liquid ground state of the S = 1/2 kagome heisenberg antiferromagnet. Science, 2011, 332: 1173–1176
8 Lee SH, Kikuchi H, Qiu Y, *et al.* Quantum-spin-liquid states in the two-dimensional kagome antiferromagnets $Zn_xCu_{4-x}(OD)_6Cl_2$. Nat Mater, 2007, 6: 853–857
9 Zhou Y, Kanoda K, Ng TK. Quantum spin liquid states. Rev Mod Phys, 2017, 89: 025003
10 Mendels P, Bert F. Quantum kagome frustrated antiferromagnets: One route to quantum spin liquids. Comptes Rendus Phys, 2016, 17: 455–470
11 Li M, Wang Q, Wang G, *et al.* Dirac cone, flat band and saddle point in kagome magnet YMn_6Sn_6. Nat Commun, 2021, 12: 3129
12 Ye L, Kang M, Liu J, *et al.* Massive Dirac fermions in a ferromagnetic kagome metal. Nature, 2018, 555: 638–642
13 Liu Z, Li M, Wang Q, *et al.* Orbital-selective Dirac fermions and extremely flat bands in frustrated kagome-lattice metal CoSn. Nat Commun, 2020, 11: 4002
14 Kang M, Ye L, Fang S, *et al.* Dirac fermions and flat bands in the ideal kagome metal FeSn. Nat Mater, 2020, 19: 163–169
15 Liu E, Sun Y, Kumar N, *et al.* Giant anomalous hall effect in a ferromagnetic kagome-lattice semimetal. Nat Phys, 2018, 14: 1125–1131
16 Okamura Y, Minami S, Kato Y, *et al.* Giant magneto-optical responses in magnetic Weyl semimetal $Co_3Sn_2S_2$. Nat Commun, 2020, 11: 4619
17 Kuroda K, Tomita T, Suzuki MT, *et al.* Evidence for magnetic Weyl fermions in a correlated metal. Nat Mater, 2017, 16: 1090–1095
18 Hu Y, Teicher SML, Ortiz BR, *et al.* Topological surface states and flat bands in the kagome superconductor CsV_3Sb_5. Sci Bull, 2022, 67: 495–500
19 Nie L, Sun K, Ma W, *et al.* Charge-density-wave-driven electronic nematicity in a kagome superconductor. Nature, 2022, 604: 59–64
20 Tanaka M, Fujishiro Y, Mogi M, *et al.* Topological kagome magnet $Co_3Sn_2S_2$ thin flakes with high electron mobility and large anomalous Hall effect. Nano Lett, 2020, 20: 7476–7481
21 Chen KY, Wang NN, Yin QW, *et al.* Double superconducting dome and triple enhancement of T_c in the kagome superconductor CsV_3Sb_5 under high pressure. Phys Rev Lett, 2021, 126: 247001
22 Fu Y, Zhao N, Chen Z, *et al.* Quantum transport evidence of topological band structures of kagome superconductor CsV_3Sb_5. Phys Rev Lett, 2021, 127: 207002
23 Gu X, Chen C, Wei WS, *et al.* Robust kagome electronic structure in the topological quantum magnets XMn_6Sn_6 (X = Dy, Tb, Gd, Y). Phys Rev B, 2022, 105: 155108
24 Uykur E, Ortiz BR, Wilson SD, *et al.* Optical detection of the density-wave instability in the kagome metal KV_3Sb_5. npj Quantum Mater, 2022, 7: 16
25 Yang SY, Wang Y, Ortiz BR, *et al.* Giant, unconventional anomalous Hall effect in the metallic frustrated magnet candidate, KV_3Sb_5. Sci Adv, 2020, 6: eabb6003
26 Fujioka J, Yamada R, Kawamura M, *et al.* Strong-correlation induced high-mobility electrons in Dirac semimetal of perovskite oxide. Nat Commun, 2019, 10: 362
27 He Y, Gayles J, Yao M, *et al.* Large linear non-saturating magnetoresistance and high mobility in ferromagnetic MnBi. Nat Commun, 2021, 12: 4576
28 Bolotin KI, Sikes KJ, Jiang Z, *et al.* Ultrahigh electron mobility in suspended graphene. Solid State Commun, 2008, 146: 351–355
29 Thomas SM, Whall TE, Parker EHC, *et al.* Improved effective mobility extraction in MOSFETs. Solid-State Electron, 2009, 53: 1252–1256
30 Ashlea Alava Y, Wang DQ, Chen C, *et al.* High electron mobility and low noise quantum point contacts in an ultra-shallow all-epitaxial metal gate $GaAs/Al_xGa_{1-x}$ as heterostructure. Appl Phys Lett, 2021, 119: 063105
31 Coldren LA, Nicholes SC, Johansson L, *et al.* High performance InP-based photonic ICs—A tutorial. J Lightwave Technol, 2011, 29: 554–570
32 Liu DF, Liang AJ, Liu EK, *et al.* Magnetic Weyl semimetal phase in a Kagomé crystal. Science, 2019, 365: 1282–1285
33 Jiao L, Xu Q, Cheon Y, *et al.* Signatures for half-metallicity and non-trivial surface states in the kagome lattice Weyl semimetal $Co_3Sn_2S_2$. Phys Rev B, 2019, 99: 245158
34 Perdew JP, Burke K, Ernzerhof M. Generalized gradient approximation made simple. Phys Rev Lett, 1996, 77: 3865–3868
35 Blöchl PE. Projector augmented-wave method. Phys Rev B, 1994, 50: 17953–17979
36 Kresse G, Joubert D. From ultrasoft pseudopotentials to the projector augmented-wave method. Phys Rev B, 1999, 59: 1758–1775
37 Souza I, Marzari N, Vanderbilt D. Maximally localized Wannier functions for entangled energy bands. Phys Rev B, 2001, 65: 035109
38 Lopez Sancho MP, Lopez Sancho JM, Sancho JML, *et al.* Highly convergent schemes for the calculation of bulk and surface green functions. J Phys F-Met Phys, 1985, 15: 851–858
39 Huang X, Zhao L, Long Y, *et al.* Observation of the chiral-anomaly-induced negative magnetoresistance in 3D Weyl semimetal TaAs. Phys Rev X, 2015, 5: 031023
40 Gao W, Zhu X, Zheng F, *et al.* A possible candidate for triply degenerate point fermions in trigonal layered $PtBi_2$. Nat Commun, 2018, 9: 3249
41 Schönemann R, Aryal N, Zhou Q, *et al.* Fermi surface of the Weyl type-II metallic candidate WP_2. Phys Rev B, 2017, 96: 121108
42 Kumar N, Sun Y, Xu N, *et al.* Extremely high magnetoresistance and conductivity in the type-II Weyl semimetals WP_2 and MoP_2. Nat Commun, 2017, 8: 1642
43 Pokharel G, Teicher SML, Ortiz BR, *et al.* Electronic properties of the topological kagome metals YV_6Sn_6 and GdV_6Sn_6. Phys Rev B, 2021, 104: 235139
44 Yuan Z, Lu H, Liu Y, *et al.* Large magnetoresistance in compensated semimetals $TaAs_2$ and $NbAs_2$. Phys Rev B, 2016, 93: 184405

Acknowledgements This work was supported by the National Key R&D Program of China (2017YFA0305400 and 2019YFA0704900), Chinese

Academy of Sciences-Shanghai Science Research Center (CAS-SSRC-YH-2015-01) and Double First-Class Initiative Fund of ShanghaiTech University. Chen Y acknowledges the support from the Engineering and Physical Sciences Research Council Platform Grant (EP/M020517/1); Guo Y acknowledges the Major Research Plan of the National Natural Science Foundation of China (NSFC, 92065201); Chen Y and Liu Z acknowledge Shanghai Municipal Science and Technology Major Project (2018SHZDZX02); Liu E acknowledges the support from the NSFC (52088101 and 11974394), and the Strategic Priority Research Program (B) of the Chinese Academy of Sciences (XDB33000000); Shi W acknowledges the support from Shanghai Committee of Science and Technology (22ZR1441800), Shanghai-XFEL Beamline Project (SBP) (3101150550588592016 1A2101001); Yang HF acknowledges the support from the NSFC (12004248) and Shanghai Sailing Program (20YF1430500); Li Y acknowledges the support from the NSFC (12104304). The calculations were carried out at the Scientific Data Analysis Platform of Center for Transformative Science and the HPC Platform of ShanghaiTech University Library and Information Services. The synchrotron-based ARPES measurement was conducted at the Beamline I05 of Diamond Light Source, and BL03U of Shanghai Synchrotron Radiation Facility. We acknowledge the Analytical Instrumentation Center of ShanghaiTech University for Laue diffraction measurements.

Author contributions Liu Z and Chen Y conceived the project; Fang H, Li Y, Xu L, and Lyu M performed the ARPES, XRD and electron transport study with the help from Yang H and Liu E; Shi W performed the theoretical calculation; Liu S and Wei L performed the STM study with the help from Wang M; Su H and Yuan J synthesized the crystals; Liu X and Yao Q performed the literature research. All authors contributed to the general discussion.

Conflict of interest The authors declare that they have no conflict of interest.

Supplementary Information Experimental details and supporting data are available in the online version of the paper.

Hongwei Fang received her BSc degree in physics from Shandong Normal University. She is currently a PhD candidate at ShanghaiTech University under the supervision of Prof. Zhongkai Liu. Her research interest focuses on studying the electronic properties of topological materials using ARPES.

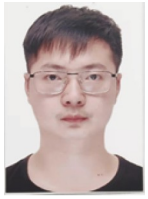

Meng Lyu obtained his PhD degree from the University of Chinese Academy of Sciences. He is now a postdoctor in Prof. Enke Liu's group at the Institute of Physics (IOP), Chinese Academy of Sciences (CAS). His research interest focuses on the exploration and study of the electrical and thermal transport properties of the magnetic topological semimetals and strongly correlated electron systems.

Wujun Shi obtained his PhD degree in physics from Nanjing University in 2013. From 2013 to 2018, he worked as Postdoctoral Research Fellow at Tsinghua University, ShanghaiTech University and Max Planck Institute for Chemical Physics of Solids (MPI-CPfS). In 2018, he joined ShanghaiTech University, and now holds the position of associate researcher. His research focuses on the electronic structure of quantum materials.

Yulin Chen is an associate professor at the Department of Physics, University of Oxford. His research interest focuses on the understanding of novel properties of quantum materials and their application. He is also interested in developing advanced ARPES instruments with new capabilities such as spin, spatial, and time resolutions.

Enke Liu obtained his PhD degree in magnetism of condensed matter physics from IOP, CAS in 2012. In the same year, he began his research career at IOP and now holds the position of Professor in physics. His research focuses on the new systems, novel states and electric/thermal transport of magnetic topological semimetals and magnetic phase-transformation materials.

Zhongkai Liu received his BSc degree in physics from Tsinghua University in 2006 and PhD degree from Stanford University in 2014. He is an associate professor at the School of Physical Science and Technology, ShanghaiTech University. His research interest focuses on characterizing the electronic structure and understanding the emergent phenomena of advanced materials with ARPES.

Kagome晶格补偿型半金属$Ni_3In_2S_2$创纪录的高迁移率和极大磁电阻现象

房红伟[1,2†], 吕孟[3†], 苏豪[1,2], 袁健[1,2], 李一苇[1], 徐丽璇[4], 刘帅[1,2], 魏立阳[1,2], 刘馨琪[1,5], 杨海峰[1], 姚岐[1,5], 王美晓[1,5], 郭艳峰[1], 史武军[6,7*], 陈宇林[1,5,8*], 刘恩克[3*], 柳仲楷[1,5*]

摘要 具有Kagome晶格的晶体有很多有趣的性质，包括受挫磁阻、电荷有序、拓扑态、超导和关联现象. 为了在电子学和自旋电子学应用中实现高性能Kagome晶格化合物，需要对能带结构仔细调整. 本文采用输运测量、角分辨光电子能谱和从头计算等方法研究了Kagome晶格晶体$Ni_3In_2S_2$的电子结构. 输运测量表明, $Ni_3In_2S_2$是一种在Kagome晶格材料中具有创纪录的高载流子迁移率(空穴和电子迁移率分别约为8683和7356 $cm^2 V^{-1} S^{-1}$)和极大磁电阻(在2 K和13 T时为15,518%)的补偿半金属. Ni在Kagome晶格中的3d电子导致的非直接带隙、小的电子/空穴口袋和大的带宽的能带结构特征很好地解释了这些特殊的性质. 这项工作表明，晶体场和掺杂是优化Kagome晶格晶体输运特性的关键因素. 我们的工作为Kagome晶格半金属在电子学和自旋电子学方面的应用提供了材料基础和优化路径.

